AGU PUBLICATIONS

JGR

Journal of Geophysical Research: Atmospheres

RESEARCH ARTICLE
10.1002/2015JD023153

Key Points:
- Arctic budget study of intermember variability
- Intermember variability fluctuates temporally and spatially
- Intermember variability is influenced by baroclinic processes

Supporting Information:
- Figures S1 and S2

Correspondence to:
A. Sommerfeld,
anja.sommerfeld@awi.de

Citation:
Sommerfeld, A., O. Nikiema, A. Rinke, K. Dethloff, and R. Laprise (2015), Arctic budget study of intermember variability using HIRHAM5 ensemble simulations, *J. Geophys. Res. Atmos.*, *120*, 9390–9407, doi:10.1002/2015JD023153.

Received 22 JAN 2015
Accepted 22 AUG 2015
Accepted article online 27 AUG 2015
Published online 28 SEP 2015

Arctic budget study of intermember variability using HIRHAM5 ensemble simulations

Anja Sommerfeld[1], Oumarou Nikiema[2], Annette Rinke[1], Klaus Dethloff[1], and René Laprise[2]

[1]Alfred Wegener Institute, Helmholtz Centre for Polar and Marine Research, Potsdam, Germany, [2]Département des Sciences de la Terre et de l' Atmosphère, Université du Québec à Montréal, Montreal, Quebec, Canada

Abstract One of the challenges in evaluating and applying regional climate models (RCMs) is the nonlinear behavior of atmospheric processes, which is still poorly understood. The nonlinearities induce chaos which leads to an internal variability in the model. Therefore, an ensemble of RCM simulations has been run and a budget study for potential temperature has been applied to investigate the internally generated variability. Hence, the physical processes associated with diabatic and dynamical terms inducing the intermember variability have been analyzed. The study is applied over the Arctic on an ensemble of 20 members, differing in their initial conditions, simulated with the RCM HIRHAM5 during summer 2012. This time period is of particular importance because of the melting sea ice and its influence on atmospheric circulation and the resulting effect on the intermember variability. The amplitude of the intermember variability of the simulations fluctuates strongly both temporally and spatially. During the beginning of August 2012 the intermember variability is strongest and coincides with the great Arctic cyclone event. The most important contributions for the intermember variability tendency are the horizontal and vertical "baroclinic" terms. Both terms have largest absolute values along the coastlines of the Arctic Ocean which are associated with the Arctic frontal zone leading to the cyclone maximum over the Arctic Ocean during summer.

1. Introduction

Regional climate models (RCMs) are sensitive to their initial conditions (ICs) due to the nonlinearities within the atmospheric dynamics [*Giorgi and Bi*, 2000; *Christensen et al*., 2001; *Caya and Biner*, 2004; *Rinke et al*., 2004; *Wu et al*., 2005; *Alexandru et al*., 2007; *Lucas-Picher et al*., 2008a, 2008b; *Roesch et al*., 2008]. *von Storch* [2005] defines the internal variability (IV) as the property of RCMs to generate different solutions for simulations, which use exactly the same lateral boundary conditions (LBCs) but differ slightly in their IC. IV should be taken into account in interpreting the results of sensitivity studies performed with RCMs [*Giorgi and Bi*, 2000]. Hence, it is of a particular importance to investigate the IV generated in RCMs. *Caya and Biner* [2004] noted that the IV of RCMs is weaker than the IV found in global climate models with magnitudes comparable to the natural climate variability.

For analyzing the IV of RCMs, ensemble simulations are performed and each ensemble member is either forced with a perturbation or is initialized with different states, leading to different solutions within the ensemble. The construction of the proper ensemble of perturbations is an intensively discussed problem in the climate modeling and numerical weather prediction (NWP) modeling [e.g., *Collins*, 2007; *Troccoli and Palmer*, 2007; *Hawkins and Sutton*, 2009; *Evans et al*., 2013; *Wan et al*., 2014]. While the investigation of RCM ensembles has been started since the mid-2000s only, considerable work has been carried out on the skill and uncertainty in NWP models since more than two decades. Different strategies of providing an ensemble of forecasts have been developed (e.g., breeding method [*Toth and Kalnay*, 1993], singular vector approach [*Buizza and Palmer*, 1995], and different data assimilation cycles [*Houtekamer et al*., 1996]). The ensemble size for the ensemble prediction is large and considers often 50 to 100 ensemble members [e.g., *Mullen and Buizza*, 2002; *Theis and Gebhardt*, 2009; *Gneiting and Raftery*, 2005; *Bonavita et al*., 2011]. *Kunii* [2014] applied an ensemble with a size of even 1000 members. Differently, the ensembles in climate simulations are much smaller and consider only few (mostly three to eight) members; this applies for global climate models (Coupled Model Intercomparison Project phase 3 (CMIP3)/CMIP5 included three- to five-member ensembles for individual models) and RCMs [e.g., *Rinke et al*., 2004; *Bellprat et al*., 2012; *Sasse and Schädler*, 2014]. However, *Alexandru et al*. [2007] demonstrated that such small ensembles do not allow a robust estimate

of RCM's internal variability. They recommended an ensemble with a minimum of 10 members to arrive at a solid estimate of IV on seasonal scale. The investigation of the IV in RCMs addresses its intensity, temporal evolution, and spatial distribution rather than the probability to cover the model's phase space. Hence, much smaller ensembles are sufficient for analyzing the IV as are necessary for the NWP.

The IV in RCMs depends on the IC, LBC, domain size, season, model parameterization, and geographical location [*Giorgi and Bi*, 2000; *Caya and Biner*, 2004; *Rinke et al*., 2004; *Wu et al*., 2005; *Alexandru et al*., 2007; *Lucas-Picher et al*., 2008a]. Diabatic and dynamic processes like convection [*Crétat and Pohl*, 2012], precipitation [*Giorgi and Bi*, 2000; *Christensen et al*., 2001], and synoptic events [*Caya and Biner*, 2004; *Alexandru et al*., 2007] influence the strength and the behavior of IV. The dependence of IV on the model domain and the corresponding synoptic conditions is obvious by comparing studies over different regions. *von Storch* [2005] summarized the midlatitudes as well-flushed regions, leading to a weak divergence between simulations differing in their IC. The Arctic as an area with weak flow through the domain is imposed to generate a stronger divergence between the simulations, because of the longer stay of baroclinic perturbations within the Arctic domain [*Rinke and Dethloff*, 2000]. Thus, in general the IV is larger in the Arctic than those for the midlatitudes [*Rinke et al*., 2004; *von Storch*, 2005]. Additionally to the location of the model domain, the size of the domain is important for the IV as well. A small domain inhibits the free development of the simulations, because they are strongly constrained by the LBC [*Giorgi and Bi*, 2000; *Rinke and Dethloff*, 2000; *Alexandru et al*., 2007].

Recently, the IV over the Arctic was investigated and compared within two different RCMs covering the same time period (Nikiema et al., submitted manuscript, 2015). It was found that the dependency of the IV on the applied model is quite weak. Both RCMs reveal the same magnitude and location of high IV.

Nikiema and Laprise [2010, 2011] (hereinafter *NL*2010, 2011) were the first who investigated the dynamical and diabatic processes which induce the IV. For this, they developed a diagnostic equation resolving the individual contributions influencing the IV tendency. *NL*2010, 2011 applied this diagnostic equation for two variables, potential temperature and relative vorticity over a region covering the eastern part of northern America and the Atlantic Ocean. The temporal evolution of IV fluctuates strongly in time and is associated with synoptic events. *NL*2010, 2011 showed that the diabatic source and sink terms deliver strongest contribution to the generation of IV, while the vertical "baroclinic" term has the same order of magnitude but contributes negatively to IV and therefore reduces it.

The aim of this study is answering the three key questions: What are the characteristics (vertical profile, temporal evolution, and spatial pattern) of IV and all the terms contributing to the IV budget in the Arctic? Which are the key terms contributing to the IV tendency? Are there and what are the differences compared to the North America region? Therefore, the diagnostic equation for potential temperature developed by *NL*2010 and applied over the northern American region is now used for a different region, namely, the Arctic. Our time period of interest is the late summer (July to September), because this season is characterized by a strong sea ice retreat in the Arctic. The large regions of open water lead to an increased exchange of moisture and heat between the ocean and the atmosphere influencing the diabatic processes [*Porter et al*., 2012; *Rinke et al*., 2013] which further influence the synoptic activity [*Jaiser et al*., 2012; *Rinke et al*., 2013]. Those processes can have an impact on IV, and the relative role of different contributions will be studied.

The 10 lowest September sea ice extents (since 1979) have all occurred in the last 10 years. We focus our analysis on summer 2012 as a representative of this "new state" of the Arctic. Through July 2012 the Arctic sea ice tracked at levels far below the average (1979–2010) as typically seen during the 2000s. On August and September 2012, the sea ice extent was at record levels, indicated by the great Arctic cyclone in August [*Simmonds and Rudeva*, 2012; *Zhang et al*., 2013; *Parkinson and Comiso*, 2013]. We use this to investigate the impact of this cyclone event on the IV.

Section 2 describes the used RCM and the experimental setup of the simulations, and section 3 presents the applied diagnostic method. The sea ice distribution and the meteorological situation during the studied time period is analyzed in section 4. In section 5 the results of the characteristics of IV (section 5.1) and of the individual contributions to IV tendency (section 5.2) are explained, whereas section 5.3 concentrates on an individual event when maximum IV occurs. The conclusions with a discussion of the obtained results are summarized in section 6.

2. Model and Simulations

In this study, the regional atmospheric RCM HIRHAM5 [*Christensen et al*., 2007] is applied. It combines the regional weather forecast model HIRLAM7 (High Resolution Limited Area Model) [*Undén et al*., 2002] and the atmospheric general circulation model European Centre/Hamburg model version 5 (ECHAM5) [*Roeckner et al*., 2003]. The HIRLAM7 provides the dynamical core and ECHAM5 the physical parameterizations for HIRHAM5. *Klaus et al*. [2012] and *Zhou et al*. [2014] were the first who applied the HIRHAM5 for the Arctic region. They analyzed spatial distributions and annual cycles for several meteorological parameters and described the ability of HIRHAM5 to simulate the observed spatial and temporal patterns.

HIRHAM5 covers the circum Arctic region (see Figure 1) with 218×200 grid cells in the horizontal and has been integrated with a spatial resolution of 25 km. In the vertical the model has 40 levels up to 10 hPa with 10 levels in the lowest 1 km. For boundary conditions the ERA-Interim reanalysis data set [*Dee et al*., 2011] provided by the European Centre for Medium-Range Weather Forecast was used to laterally drive HIRHAM5. The surface pressure and the temperature, the horizontal wind components, specific humidity, cloud water, and cloud ice in each vertical level were updated every 6 h. Further, ERA-Interim is used to initialize HIRHAM5 and to provide the lower boundary conditions with the daily sea surface temperature (SST) and sea ice concentration. The sea ice thickness is set constant to 2 m in HIRHAM5. The model output is saved every 6 h and for 19 pressure levels in the vertical: 10, 30, 50, 70, 100, 200, 250, 300, 400, 500, 600, 700, 800, 850, 900, 925, 950, 975, and 1000 hPa.

To analyze and quantify the intermember variability of HIRHAM5 it is important to run the model without any internal nudging, as recommended by *Alexandru et al*. [2007]. As discussed in the Introduction, the number of simulations belonging to an ensemble needs to be large enough to reach a stable estimation of the model's internal variability. *Alexandru et al*. [2007] proved by RCM experiments where they progressively increased the ensemble size that an ensemble of 20 3 month long RCM simulations is appropriate for studying the RCM's IV. Therefore, we follow their approach in accordance with other studies [*NL*2010, 2011; *O'Brien et al*., 2011] and use an ensemble with 20 members running with the same LBC and which differ only in their atmospheric IC. This is arranged by a different initialization time that was shifted successive by 6 h in each case. This method follows previous studies [e.g., *Rinke et al*., 2004; *Alexandru et al*., 2007; *NL*2010, 2011] and is reasonable to study the RCM's IV and its consequences on seasonal climate statistics. The first simulation starts on 1 July 2012 at 00:00 UTC, the second starts on 1 July at 06:00 UTC, the third starts on 1 July at 12:00 UTC, and the last simulation starts on 5 July 2012 at 18:00 UTC. Each simulation runs continuously until 30 September 2012. The analysis is applied for the time period that is covered by all ensemble members from 6 July to 30 September 2012. The year of interest is 2012 due to the strong negative sea ice anomaly in this summer. To perform the budget study for the potential temperature additional variables such as the temperature tendencies due to radiation, vertical diffusion, condensation, and convection have been written out in HIRHAM5. The tendencies are stored every 6 h on 19 pressure levels.

3. Method

The applied equation of the intermember variability (IV) budget study for potential temperature was developed and described in detail in *NL*2010, 2011, and it is summarized here in a short description. The internal variability is described by the cross-ensemble spread and calculated by the intermember variance σ^2 of the 20 ensemble members for the variable φ.

$$\sigma_\varphi^2 \approx \frac{1}{N}\sum_{n=1}^{N}(\varphi_n - \langle\varphi\rangle)^2 \equiv \langle\varphi'^2_{\mathrm{n}}\rangle \tag{1}$$

The index n represents each individual member of the ensemble, and N is the total number of the ensemble members, 20 in this case. Parameter $\langle\varphi\rangle$ is the ensemble mean, and φ_n' is the deviation of the variable φ from the ensemble mean.In this study the budget equation for the potential temperature

$$\theta = T\left(\frac{p_0}{p}\right)^{\frac{R}{c_p}} \tag{2}$$

with the temperature T, the pressure p, the reference pressure p_0 of 1000 hPa, R the gas constant for dry air, and c_p the specific heat of dry air, is used. The initial equations for the development of the potential temperature

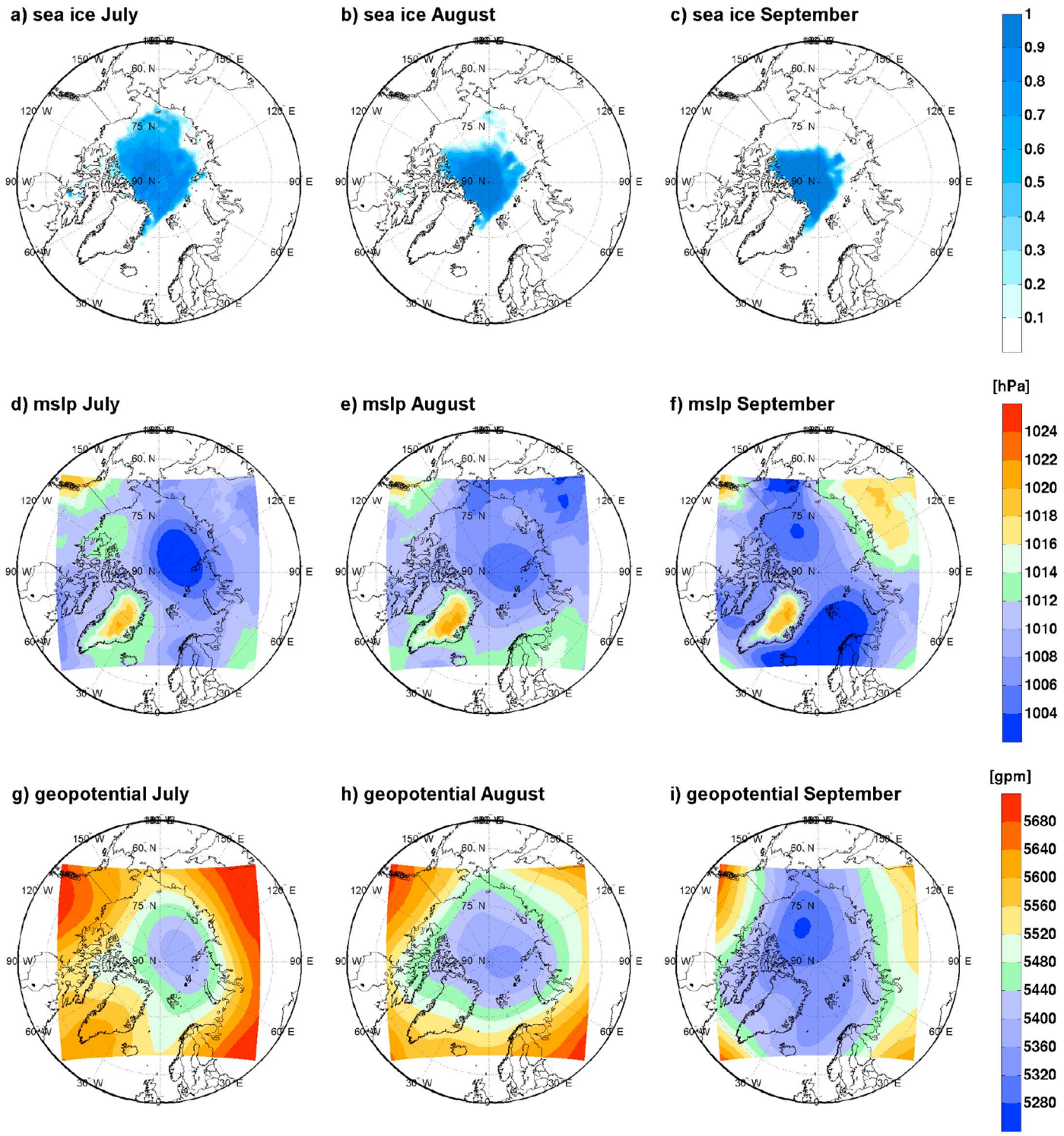

Figure 1. (first row) Monthly mean of sea ice concentration, (second row) mean sea level pressure (mslp) in hPa, and (third row) geopotential height at 500 hPa in gpm for (first column) July, (second column) August, and (third column) September 2012. (a–c) ERA-Interim and (d–i) ensemble average of the 20 HIRHAM5 simulations.

budget equation are the first law of thermodynamics and the mass-continuity equation in vertical pressure coordinates for potential temperature, and they can be combined for each ensemble member n as

$$\frac{\partial \theta_n}{\partial t} + \vec{\nabla} \cdot \left(\theta_n \vec{V}_n \right) + \frac{(\theta_n \omega_n)}{\partial p} = J_n. \tag{3}$$

$\vec{V}_n$ is the horizontal wind, and ω_n is the vertical wind component. J_n represents the source and sink terms, describing the diabatic heating rate and involves the heating due to radiation, vertical diffusion and surface sensible heat flux, convection, and condensation. The ensemble-mean operator ($<>$) is applied in equation (3) to obtain the prognostic equation for the ensemble mean potential temperature

$$\frac{\partial\langle\theta\rangle}{\partial t}+\vec{\nabla}\cdot\left\langle\theta\vec{V}\right\rangle+\frac{\partial\langle\theta\omega\rangle}{\partial p}=\langle J\rangle. \tag{4}$$

Subtracting equation (4) from equation (3) leads to the prognostic equation of the deviation of the potential temperature:

$$\frac{\partial\theta_n'}{\partial t}+\vec{\nabla}\cdot\left(\theta_n\vec{V}_n-\left\langle\theta\vec{V}\right\rangle\right)+\frac{\partial(\theta_n\omega_n-\langle\theta\omega\rangle)}{\partial p}=J_n'. \tag{5}$$

The application of the Reynolds decomposition rules and the $\vec{\nabla}$ −rules results in

$$\begin{aligned}&\frac{\partial\theta_n'}{\partial t}+\langle\theta\rangle\vec{\nabla}\cdot\vec{V}_n'+\vec{V}_n'\cdot\vec{\nabla}\langle\theta\rangle+\theta_n'\vec{\nabla}\cdot\left\langle\vec{V}\right\rangle+\left\langle\vec{V}\right\rangle\cdot\vec{\nabla}\theta_n'+\vec{\nabla}\cdot\left(\theta_n'\vec{V}_n'-\left\langle\theta_n'\vec{V}_n'\right\rangle\right)\\&+\langle\theta\rangle\frac{\partial\omega_n'}{\partial p}+\omega_n'\frac{\partial\langle\theta\rangle}{\partial p}+\theta_n'\frac{\partial\langle\omega\rangle}{\partial p}+\langle\omega\rangle\frac{\partial\theta_n'}{\partial p}+\frac{\partial}{\partial p}\left(\theta_n'\omega_n'-\langle\theta_n'\omega_n'\rangle\right)=J_n'\end{aligned} \tag{6}$$

The validity of the mass-continuity equation leads to the fact that second and seventh terms and the fourth and ninth terms cancel each other. Then the Euler decomposition has been used. Further, a multiplication by θ_n', an additional ensemble averaging and the application of the approach of equation (1) to replace $\varphi_n'^2$ by the IV, has been applied. Hence, the prognostic equation of potential temperature variance is written as

$$\begin{aligned}&\frac{1}{2}\frac{D\sigma_\theta^2}{Dt}\equiv\frac{\partial}{\partial t}\left[\frac{\sigma_\theta^2}{2}\right]+\left\langle\vec{V}\right\rangle\cdot\vec{\nabla}\frac{\sigma_\theta^2}{2}+\langle\omega\rangle\frac{\partial}{\partial p}\left[\frac{\sigma_\theta^2}{2}\right]\\&=-\left\langle\theta_n'\vec{V}_n'\right\rangle\cdot\vec{\nabla}\langle\theta\rangle-\langle\theta_n'\omega_n'\rangle\frac{\partial\langle\theta\rangle}{\partial p}-\left\langle\theta_n'\vec{\nabla}\cdot\left(\theta_n'\vec{V}_n'\right)\right\rangle-\left\langle\theta_n'\frac{\partial}{\partial p}(\theta_n'\omega_n')\right\rangle+\langle\theta_n'J'\rangle_n.\end{aligned} \tag{7}$$

By calculating $\left[(7)+\frac{1}{2}\sigma_\theta^2\left(\vec{\nabla}\cdot\left\langle\vec{V}\right\rangle+\frac{\partial\langle\omega\rangle}{\partial p}=0\right)\right]$, the diagnostic potential temperature IV tendency in flux form is obtained with the following contributions:

$$\frac{\partial\sigma_\theta^2}{\partial t}=A_h+A_v+B_h+B_v+C+E_h+E_v. \tag{8}$$

with

$$A_h=-\vec{\nabla}\cdot\left(\left\langle\vec{V}\right\rangle\sigma_\theta^2\right) \tag{9}$$

$$A_v=-\frac{\partial\left(\langle\omega\rangle\sigma_\theta^2\right)}{\partial p} \tag{10}$$

$$B_h=-2\left\langle\theta_n'\vec{V}_n'\right\rangle\cdot\vec{\nabla}\langle\theta\rangle \tag{11}$$

$$B_v=-2\langle\theta_n'\omega_n'\rangle\frac{\partial\langle\theta\rangle}{\partial p} \tag{12}$$

$$C=2\langle\theta_n'J_n'\rangle \tag{13}$$

$$E_h=-2\left\langle\theta_n'\vec{\nabla}\cdot\left(\theta_n'\vec{V}_n'\right)\right\rangle \tag{14}$$

$$E_v=-2\left\langle\theta_n'\frac{\partial}{\partial p}(\theta_n'\omega_n')\right\rangle. \tag{15}$$

The left-hand side of equation (8) is the diagnostic potential temperature IV tendency, and on the right-hand side its local changes by seven contributions are listed. The particular contributions describe different atmospheric processes. The terms A_h and A_v are the horizontal and vertical transport terms for the generation of the IV of potential temperature by the ensemble-mean flow. The terms B_h and B_v are the covariances of

potential temperature acting upon ensemble-mean gradients in the horizontal and vertical and are related to baroclinic processes in the weather systems and linked to synoptic events. Therefore, they are called baroclinic terms hereinafter. C is the diabatic source and sink term and includes temperature tendencies due to radiation, vertical diffusion and surface sensible heat flux, condensation, and convection which are summarized in J_n. The terms E_h and E_v are the third-order terms, meaning the covariance of the potential temperature acting upon the perturbation gradient.

The horizontal diffusion represents a subgrid-scale process and is not considered in this budget study, because its influence is weak. Its contribution to the diabatic source and sink term C is $-0.3 \times 10^{-5} \mathrm{K}^2/\mathrm{s}$ at the surface and almost zero in the upper troposphere.

To avoid incorrect values of the lower pressure levels over the mountain regions, the fields are masked out in the grid cells of those pressure levels that are affected by the orography. Further, values in the 15-grid-cell-wide boundary zone are neglected, because the IV is small due to the same LBCs that are used for all simulations. The boundary zone is also not considered for the spatial averages. In addition, the patterns of the spatial distributions are graphically smoothed. The smoothing is based on a running mean of 11×11 grid cells to reduce noise on small scales and allowing an easier interpretation. The vertical averages are based on a vertical integration of the 12 pressure levels between the bottom and 300 hPa.

4. Sea Ice and Meteorological Conditions During the Study

For a better understanding of the results of the IV budget study for the Arctic, the sea ice concentration and the atmospheric circulation patterns are shown for July, August, and September 2012 (Figure 1). The monthly mean sea ice concentration is based on ERA-Interim, and the mean sea level pressure (mslp) and the geopotential height at 500 hPa are an ensemble mean of the 20 ensemble simulations. The strongest sea ice retreat is observed during July in the Laptev and Beaufort Seas (Figure 1a compared to Figure 1b) and the whole Eastern Arctic and Pacific Sector of the Arctic Ocean were ice free by September 2012 (Figure 1c). The mslp and the geopotential height reveal the circumpolar circulation except from the mslp on September. During the season the low-pressure system changes its intensity. On July and August extensive low pressure is found over the Arctic Ocean and Siberia. On September the tropospheric pressure system over the Arctic split into two centers and high pressure over Siberia was formed.

The summer season of 2012 was embossed by the great Arctic cyclone of August 2012 [*Zhang et al*., 2013] that developed on 2 August over northern Siberia and entered the East Siberian Sea on 4 August and reached its maximum on 6 August with a minimum central pressure of 966 hPa [*Simmonds and Rudeva*, 2012; *Zhang et al*., 2013; *Parkinson and Comiso*, 2013]. The cyclone persisted almost 13 days and had strong impact on the sea ice, with enhanced melting and decreased thickness in the Canadian Basin due to increased upward ocean heat transport caused by the strong winds and associated ice motion [*Zhang et al*., 2013].

5. Results

In the following the potential temperature IV and its contributions are analyzed calculating the vertical profiles, the temporal evolution, and the spatial distribution. The time period considered is 6 July to 30 September 2012. The results are shown from 1000 hPa up to 300 hPa, because the focus is on the troposphere.

5.1. Quantification of IV

First, the IV of potential temperature is analyzed to identify time periods and regions within the Arctic domain and in vertical levels of high and low IV. The vertical profile for the time- and domain-averaged potential temperature IV is shown in Figure 2a. The largest value is observed at 500 hPa, and a second maximum occurs at 900 hPa to 925 hPa. The smallest values of IV are simulated near the surface, because of the same lower boundary forcing for all ensemble members, and at 300 hPa. In order to further analyze the maxima and minima obtained by the vertical profile, Figure 2b presents the time evolution of the domain-averaged potential temperature IV at 925 hPa, 500 hPa, and 300 hPa. Besides, the vertical mean of IV is shown. As expected based on Figure 2a the highest potential temperature IV occurs at 500 hPa and the lowest mostly near 300 hPa. Moreover, IV fluctuates strongly in time from $3\,\mathrm{K}^2$ to $9\,\mathrm{K}^2$ (vertical average) and from $4\,\mathrm{K}^2$ to $14\,\mathrm{K}^2$ (at 500 hPa). During the analyzed time period IV reaches at all pressure levels highest values between

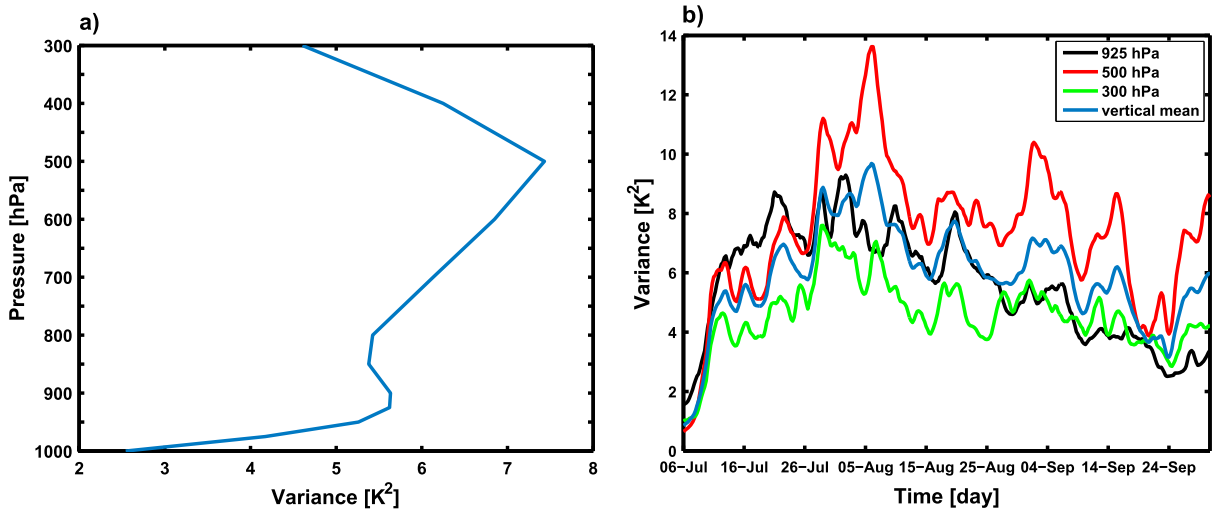

Figure 2. (a) Vertical profile of the temporal and domain-averaged intermember variability in K^2 and (b) temporal evolution of the domain-averaged intermember variability in K^2 at 925 hPa, 500 hPa, 300 hPa, and the vertical average.

27 July and 9 August with an absolute maximum of almost 14 K^2 at 500 hPa on 5 August 2012 at 06:00 UTC. This result coincides with the great Arctic cyclone of August 2012 [*Zhang et al.*, 2013]. Lowest values of IV occur during 19 and 24 September of nearly 4 K^2 at 500 hPa.

The temporal and vertical averaged spatial pattern of IV and the spatial pattern at 925 hPa, 500 hPa, and 300 hPa are shown in Figure 3. Due to the fixed lateral boundary forcing IV is small near the boundaries of the model domain. Again, the highest IV occurs at 500 hPa (Figure 3c) with maximum values of 12 K^2 over the Arctic Ocean. At 925 hPa (Figure 3b) two centers of high potential temperature IV can be noted over the East Siberian/Laptev Sea and Beaufort Sea areas. It is obvious that the locations of maximum IV and its intensities change with height. Therefore, the vertical averaged pattern (Figure 3a) is quite homogeneous without any pronounced local maxima and minima. Table 1 summarizes the domain-averaged values for the IV of potential temperature.

5.2. Contributions to IV

In this section, the different contributions to the IV tendency of potential temperature (left-hand side in equation (8)) are investigated. Therefore, the characteristics of the seven terms explained in equations 9–15 are analyzed with respect to their overall importance and specific magnitude, pattern, and variability.

The temporal and spatial averaged vertical profile for each contribution (Figure 4) identifies strongest influence on the IV tendency due to the horizontal (B_h) and vertical baroclinic (B_v) terms. B_h has positive values in all vertical levels and therefore contributes to a generation of IV and can be interpreted as a source term for IV. According to equation (11), B_h contributes positively to the IV tendency, when the covariance between the perturbations of the potential temperature and the horizontal wind $(\langle \theta_n^{'} \vec{V_n^{'}} \rangle)$ and the horizontal gradient of the mean potential temperature $(\vec{\nabla} \langle \theta \rangle)$ have a contrary sign. The potential temperature of the ensemble mean increases southward $(\vec{\nabla} \langle \theta \rangle < 0)$, and therefore, the covariance is positive $(\langle \theta_n^{'} \vec{V_n^{'}} \rangle > 0)$. Physically, this means that cold air fluctuations $(\theta_n^{'} < 0)$ flow toward the warmer southern region $(\vec{V_n^{'}} < 0)$ or warm air fluctuations $(\theta_n^{'} > 0)$ flow toward the northern colder regions $(\vec{V_n^{'}} > 0)$. Hence, a flow against the horizontal gradient of the ensemble mean of the potential temperature $(\vec{\nabla} \langle \theta \rangle < 0)$ results in a generation of the potential temperature IV. In contrast, the values of B_v (equation (12)) are always negative, indicating a reduction of the potential temperature IV. The covariances between the fluctuations of the potential temperature and the vertical wind component $(\langle \theta_n^{'} \omega_n^{'}, \rangle)$ and the vertical gradient of the ensemble mean potential temperature $\left(\frac{\partial \langle \theta \rangle}{\partial p}\right)$ have the same sign. $\left(\frac{\partial \langle \theta \rangle}{\partial p}\right)$ is always negative due to the atmosphere's stable mean state. Therefore,

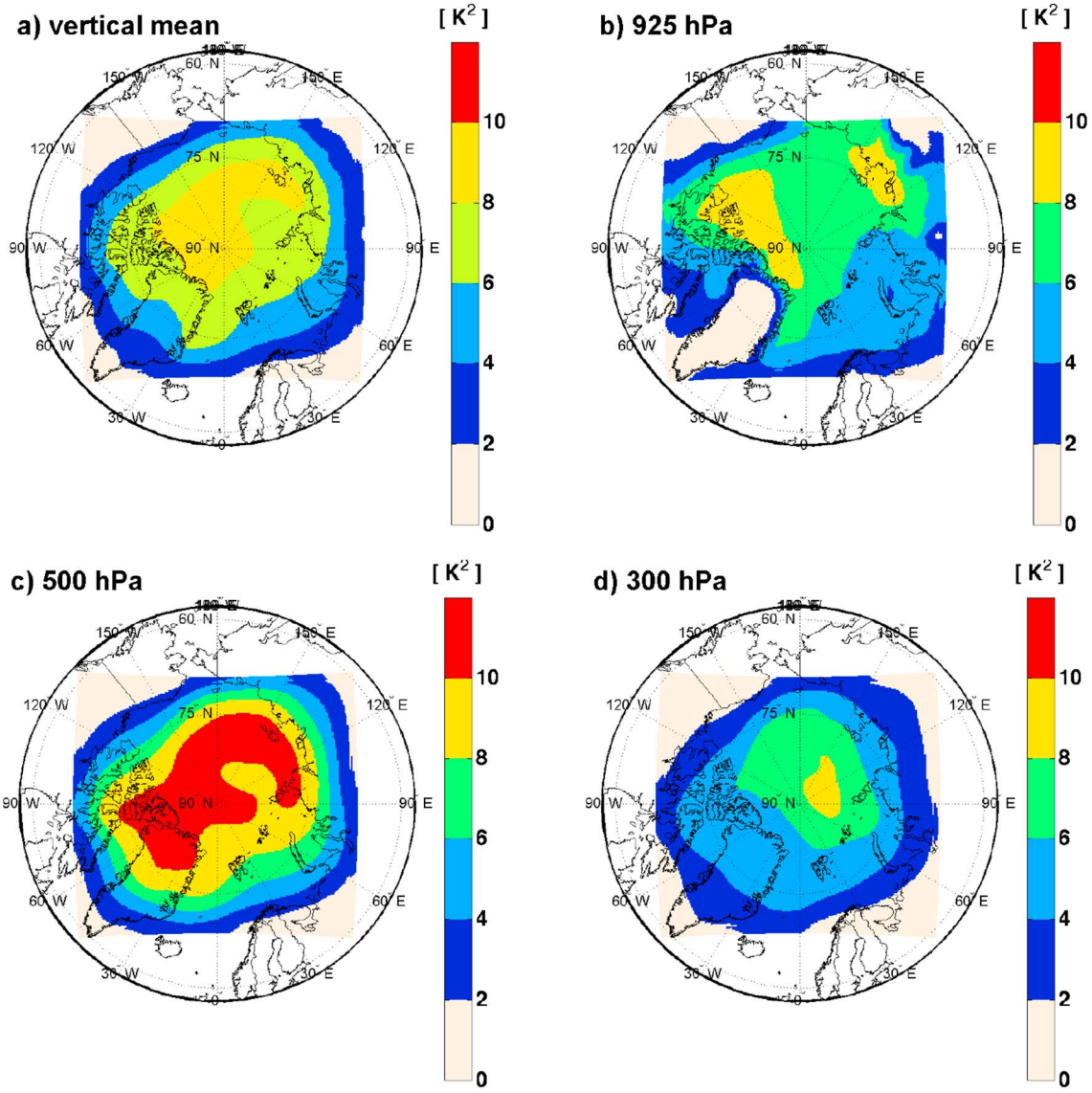

Figure 3. (a) Temporal and vertical averaged intermember variability in K^2 and (b) temporal averaged intermember variability in K^2 at (b) 925 hPa, (c) 500 hPa, and (d) 300 hPa.

$(\theta_n'\omega_n')$ is negative, indicating ascending $(\omega_n' < 0)$ warm air fluctuations $(\theta_n' > 0)$ and descending $(\omega_n' > 0)$ cold air fluctuations $(\theta_n' < 0)$. These motions coincide with the ensemble mean flow and result in a reduction of potential temperature IV. Similar to IV, the magnitude of the contributions depends on the height and is smallest in the middle and at the top of the troposphere for B_h. Maxima of B_h are calculated at 975 hPa (approximately $8 \times 10^{-5}\mathrm{K}^2/\mathrm{s}$) and at 400 hPa (approximately $7 \times 10^{-5}\mathrm{K}^2/\mathrm{s}$). The magnitude of B_v is vertically more uniform (approximately $-5 \times 10^{-5}\mathrm{K}^2/\mathrm{s}$ to $-4 \times 10^{-5}\mathrm{K}^2/\mathrm{s}$) between 900 hPa and 400 hPa. Further, B_v is of no importance at the surface and near the tropopause, because the vertical wind velocity is almost zero at these levels. The other terms (apart from C) are 100 times smaller compared to B_h and B_v and fluctuate around zero, hence contribute positively and negatively to the IV tendency depending on the level. Due to the increasing horizontal wind velocity with increasing heights, the magnitude of the transport term A_h is enhanced in the upper levels. Above 900 hPa A_h contributes negatively to IV tendency, leading to a reduction of IV. The diabatic source and sink term C changes its sign with respect to the vertical levels. C stands for the covariance between potential temperature perturbation and the perturbation of the diabatic heating rate (equation (13)). A generation of potential temperature IV is detected when warm air fluctuations $(\theta_n' > 0)$

Table 1. Domain-Averaged Intermember Variability (IV in K^2) for Potential Temperature and All Terms in $\times 10^{-5}$ K^2/s (See Section 3) Contributing to Its Temporal Change

	Temporal Average							Vertical Average on 5 August at 06:00 UTC
Terms	Vertical Average	At 1000 hPa	At 925 hPa	At 800 hPa	At 700 hPa	At 500 hPa	At 300 hPa	
IV	6.00	2.54	5.62	5.43	6.13	7.43	4.61	9.48
Ah	−0.48	−0.37	0.11	−0.19	−0.48	−0.86	−0.94	−1.16
Av	−0.02	−0.05	−0.03	0.10	0.10	−0.12	−0.00	−0.05
Bh	5.02	6.16	6.46	3.76	3.75	5.69	3.21	11.76
Bv	−4.24	−0.52	−3.99	−4.21	−4.51	−5.33	−1.42	−8.88
Eh	−0.10	0.02	−0.05	−0.26	−0.24	−0.03	0.29	0.81
Ev	0.07	−0.26	−0.13	0.58	0.22	0.25	0.12	−0.03
C	0.09	−4.33	−0.61	1.43	2.15	2.05	−0.38	0.40
Sum of all Terms	1.15	1.38	1.76	1.21	0.99	1.14	0.87	2.88

are heated diabatically $(J_n' > 0)$. C contributes to a reduction of IV tendency, when warm perturbations are cooled or cold perturbations are heated. Near the ground, C is negative with values around $-4 \times 10^{-5} K^2/s$. This is caused by the temperature tendency due to condensation contributing negatively to the term C and that is not fully compensated by the temperature tendencies due to the radiation and the vertical diffusion that have a positive impact on term C. We found that C contributes positively to the IV tendency of potential temperature in the midtroposphere, since the temperature tendencies due to condensation and radiation are positive above 800 hPa. The vertical profile of the sum of all the calculated contributions is slightly positive (approximately $1 \times 10^{-5} K^2/s$), whereas in fact, there is no net tendency of IV. This is due to the neglect of several small dissipative mechanisms that are acting in the model, either implicitly in the numeric or explicitly such as horizontal diffusion that is neglected. We found that the mismatch between the IV tendency and the sum of all terms is quite large compared to the results obtained for the midlatitude region [*NL*2010, 2011]. Therefore, it is assumed that the errors depend on the model domain. The balance between the IV tendency and the sum of all terms can be improved by including dissipative terms. A more detailed analysis of the numerical errors and the dependency on the model domain is planned as future work. Details concerning the behavior of each contribution depending on the level are presented in Table 1.

The temporal evolution for each contribution (vertical and domain averaged) is shown in Figure 5a. Again, B_h and B_v account most strongly to IV tendency, with B_h overall positive and B_v negative. The term C is mostly positive. The other terms fluctuate around zero, because their contribution to IV tendency is in general small (A_v and E_v) or they are balanced over the model domain (with local regions of positive and negative values) (A_h and E_h). It has to be emphasized that the contributions significantly fluctuate in time. Apart from some negative peaks the sum of all terms (Figure 5a) is positive due to the strong positive contribution of B_h and C which are not fully balanced by B_v. Figures 5b–5d illustrate the temporal evolution of the seven contributions to the IV tendency at 925 hPa, 500 hPa, and 300 hPa. At all levels B_h has the strongest and always positive contribution to the potential temperature IV tendency. This positive contribution is associated with a generation of IV. However, the values become smaller with increasing height. At 925 hPa and

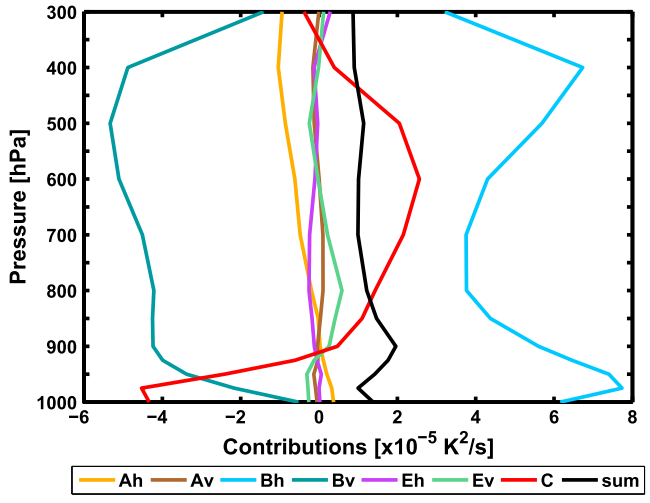

Figure 4. Vertical profiles of the seven temporal and domain-averaged contributions in $10^{-5} K^2/s$ to intermember variability tendency and the sum of all contributions.

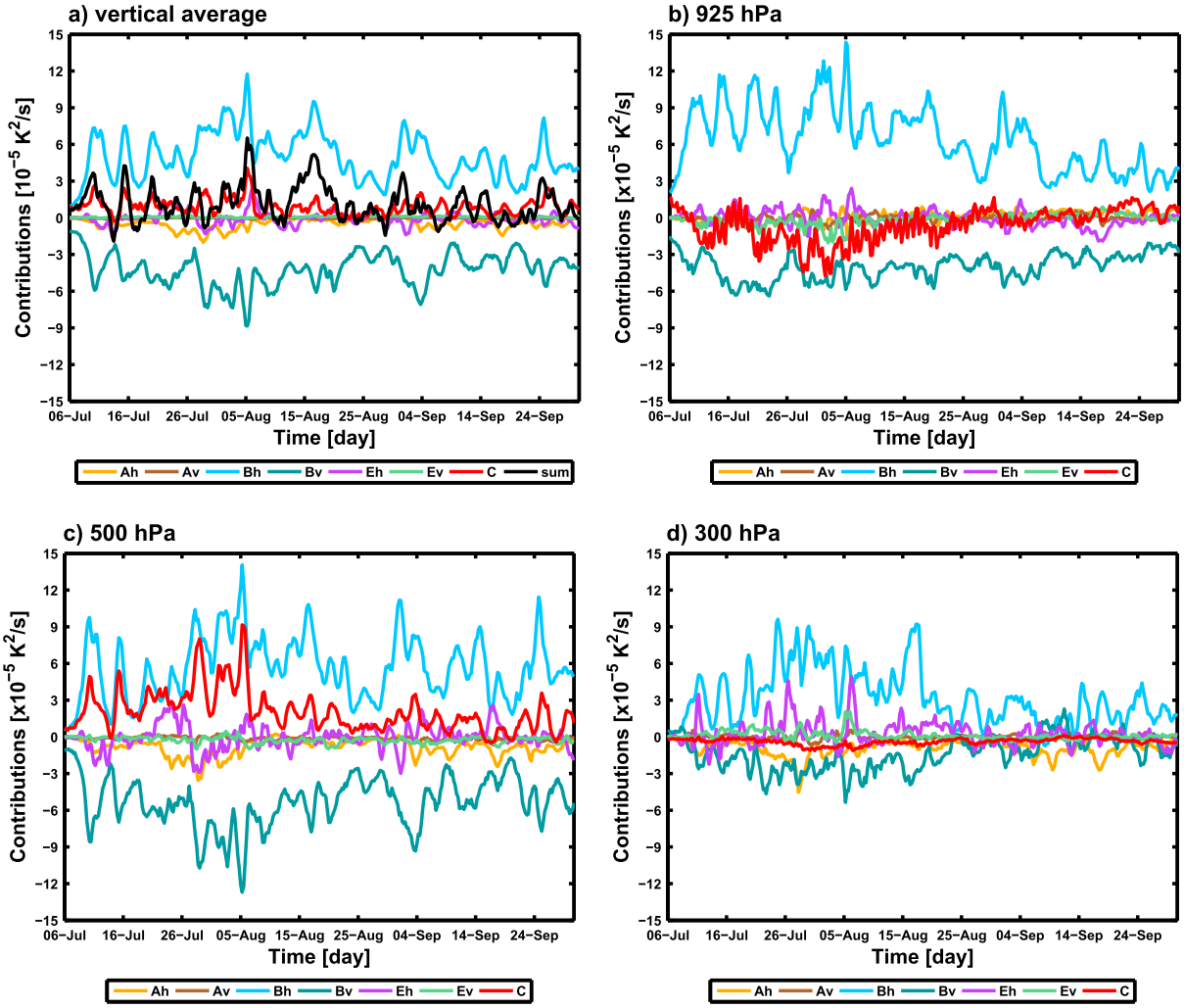

Figure 5. (a) Temporal evolution of the seven domain-averaged contributions in $10^{-5}K^2/s$ to intermember variability tendency for the vertical average, at (b) 925 hPa, at (c) 500 hPa, and at (d) 300 hPa. In Figure 5a the sum of all contributions is included.

500 hPa the values reach approximately $7\times10^{-5}K^2/s$, and at 300 hPa they are reduced to $4\times10^{-5}K^2/s$ on average. The vertical baroclinic term (B_v) has a negative contribution to potential temperature IV tendency during the whole time period at 925 hPa and 500 hPa and also mostly at 300 hPa. This negative contribution leads to a reduction of the IV. At 925 hPa and at 300 hPa the magnitude of B_v is smaller than B_h and there are short time periods when B_v reaches even positive values at 300 hPa. The sign of term C differs with the height level and has highest absolute values during the end of July and the beginning of August (coinciding with the strongest sea ice reduction) at 925 hPa and 500 hPa. As shown in Figure 4 the horizontal transport term A_h becomes more important with increasing height and is negative above 925 hPa. The magnitudes of E_h and E_v depend strongly on time. Both terms can fluctuate around zero or peak out positively and negatively. In upper levels the peaks reach highest values with up to $5\times10^{-5}K^2/s$ at 300 hPa.

The comparison of the temporal evolution of the IV (Figure 2b) and of the individual contributions (Figure 5) illustrates for some cases a coinciding increasing intensity like during the period from 27 July to 9 August 2012. Especially, B_h and B_v indicate a correlation with IV, more precisely $R=0.59$ between IV and B_h and $R=-0.69$ between IV and B_v (based on the vertical and domain-averaged time series). This is not unexpected, because B_h is the horizontal baroclinic term, associated with synoptic activity that influences the behavior of IV [*Giorgi and Bi*, 2000; *Lucas-Picher et al.*, 2008a; *Alexandru et al.*, 2007; *NL*2010, 2011].

Figure 6 illustrates the spatial distribution of the temporal and vertical averaged contributions to IV tendency by the different terms. Again, positive values mean an increase and negative values a reduction of potential temperature IV, indicating sources and sinks for IV, respectively. Pronounced regionally different patterns are obvious for the different terms.

The horizontal and vertical transport terms A_h and A_v have negative and positive values (Figures 6a and 6b) and therefore can produce and reduce IV depending on the region by moving the IV. However, the magnitude of A_h is 100 times higher than A_v. The negative values of A_h are mainly located over the Arctic Ocean (with maxima over the Beaufort Sea) and Greenland, illustrating regions that loose IV toward regions of positive A_h or out of the model domain. The positive contribution to IV tendency, resulting in a generation, occurs mostly over the land areas, indicating a transport of IV toward these regions. Regions that are characterized by an intense production of IV due to the transport into the model domain are mostly found over eastern Siberia and the Greenland Sea. Several studies identify these regions as centers of originating cyclones (e.g., East Siberia) [*Serreze et al.*, 2001] and of high cyclone center counts (e.g., Greenland Sea) [*Serreze and Barrett*, 2008]. Unlike A_h, the positive values of A_v are more widespread and occur over the Atlantic side of the Arctic and all land (apart from Greenland). Negative contributions arise over the central Arctic Ocean and Greenland.

The horizontal baroclinic term B_h (Figure 6c) contributes overall positively to IV tendencies. Maximum values reaching $7\times10^{-5}\mathrm{K}^2/\mathrm{s}$ and higher are located at the coast of Laptev/East Siberian Sea and over the Barents Sea. Smallest contributions are calculated over the central Arctic Ocean. In contrast to B_h, B_v (Figure 6d) contributes to a reduction of IV. The region along the Russian coast reveals strongest negative contribution of up to $-7\times10^{-5}\mathrm{K}^2/\mathrm{s}$. Weakest absolute contributions of B_v to IV tendency are found over the land, especially over Alaska and Greenland. B_h and B_v contribute strongest along the Russian coast coinciding with the region of high Eady growth rate (see Figure S1 in the supporting information) that was simulated with the HIRHAM5 between 850 hPa and 500 hPa.

The magnitude of the contribution of the third-order terms E_h and E_v (Figures 6e and 6f) differs in an order of 100, but both contribute to a generation and a reduction of IV in dependence on the location. The vertical and temporal averaged contribution of E_h is mainly limited to the Arctic Ocean and seldom reaches values of $\pm4\times10^{-5}\mathrm{K}^2/\mathrm{s}$. E_v contributes almost overall positively to the IV tendency with highest values over the ocean (approximately $0.13\times10^{-5}\mathrm{K}^2/\mathrm{s}$). The negative values are located mostly at some coastlines and East Siberia.

The impact of the temporal and vertical averaged diabatic source and sink term C (Figure 6g) is 10 times smaller compared to the one of A_h, B_h, and E_h. This can be explained by the positive and negative contributions that are compensating each other in the vertical as shown in Figure 4. Small reductions of IV occur over the Beaufort Sea, Fram Strait, and at the coastlines of Greenland. Over most other areas, C contributes to a generation of IV.

The sum of all terms (Figure 6h) shows a positive IV tendency, illustrating a generation of IV over Eastern Russian Arctic, Baffin Bay, and Greenland Sea. Negative values arise over the Arctic Ocean, Alaska, and Western Russian Arctic.

As detected for the domain-averaged analysis, both baroclinic terms B_h and B_v are the most important contributions. Therefore, their spatial distribution with respect to different vertical levels is analyzed more deeply (Figure 7). The horizontal baroclinic term B_h is positive overall and has its maximum at 925 hPa. Along the coastlines B_h reaches values higher than $13\times10^{-5}\mathrm{K}^2/\mathrm{s}$. In other areas, the values range between $1\times10^{-5}\mathrm{K}^2/\mathrm{s}$ and $7\times10^{-5}\mathrm{K}^2/\mathrm{s}$. With increasing height, the magnitudes become weaker, and at 300 hPa B_h has values lower than $7\times10^{-5}\mathrm{K}^2/\mathrm{s}$, but the spatial patterns (locations of the maxima) are quite similar at all height levels.

Like B_h, the term B_v (Figures 7b, 7d, and 7f) reveals similar spatial patterns with highest contribution along the coastlines. However, its sign is negative, indicating a reduction of IV. The impact of B_v is weaker (mostly $<9\times10^{-5}\mathrm{K}^2/\mathrm{s}$ and rarely $>11\times10^{-5}\mathrm{K}^2/\mathrm{s}$) compared to B_h. Between the lower and the midtropospheric levels, the intensity of the magnitudes over the Arctic Ocean ranges between $-1\times10^{-5}\mathrm{K}^2/\mathrm{s}$ to $-5\times10^{-5}\mathrm{K}^2/\mathrm{s}$ (at 925 hPa) to approximately $-7\times10^{-5}\mathrm{K}^2/\mathrm{s}$ at 500 hPa. At upper tropospheric levels the

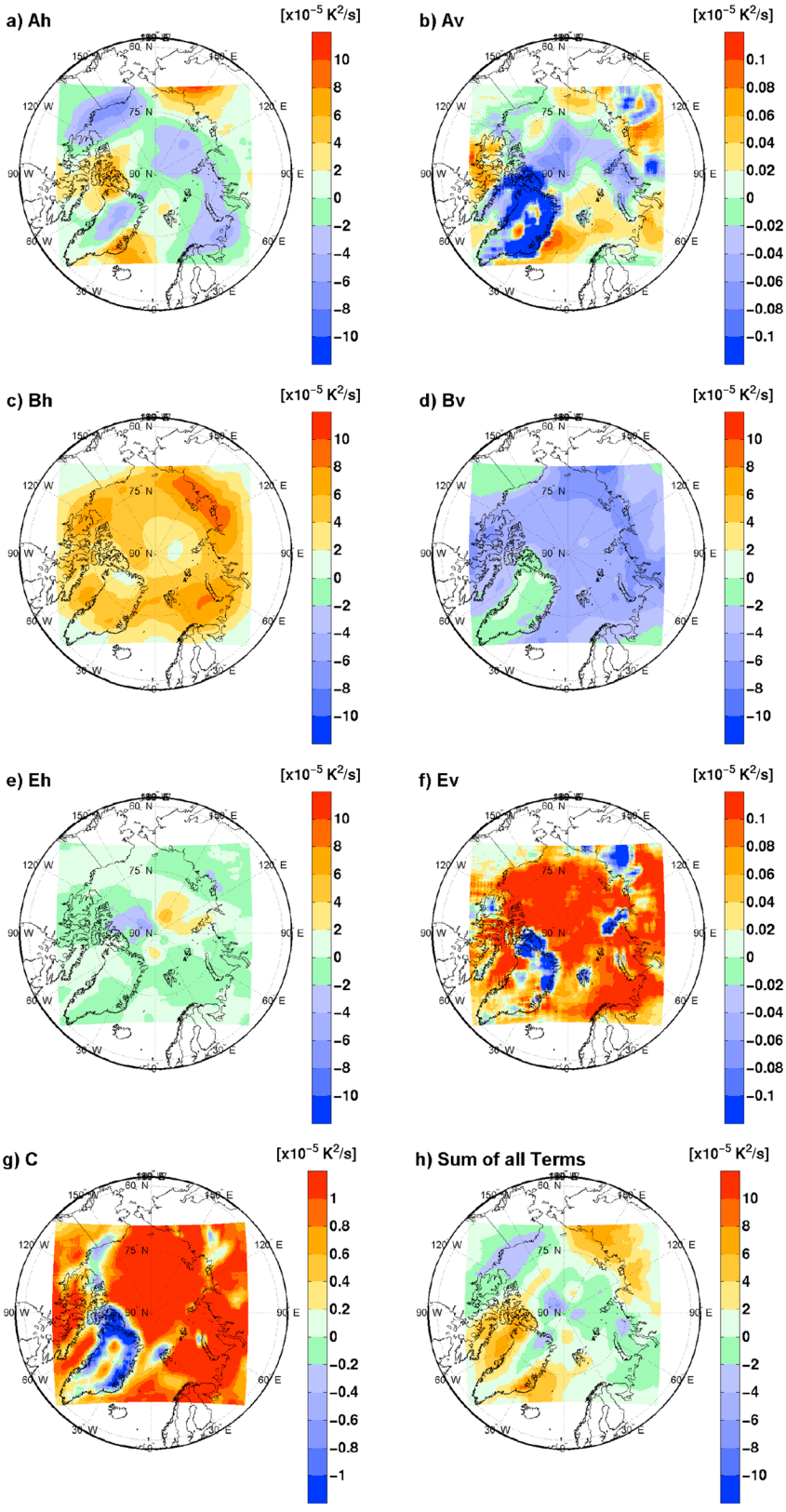

Figure 6. (a–g) Temporal and vertical averages of the seven contributions in 10^{-5}K^2/s to intermember variability tendency and (h) the sum of all contributions in 10^{-5}K^2/s. The contribution C is 10 times, and A_v and E_v are 100 times smaller than the other contributions; therefore, the color bars are adapted.

impact of B_v to IV tendency of potential temperature becomes weaker and rarely reaches values of $-5\times10^{-5}K^2/s$. In contrast, B_h is still significant at upper levels with values ranging from $1\times10^{-5}K^2/s$ to $9\times10^{-5}K^2/s$, also shown in Table 1.

However, the spatial distributions (Figures 6 and 7) reveal that A_h reaches the same magnitude as the baroclinic terms but contributes positively and negatively to IV depending on the region. Therefore, the spatial average leads to a cancelation of A_h, resulting in small values considering the vertical profile and temporal evolution (Figures 4 and 5). From this it is also obvious that the sum of all contributions (Figure 6h) provides a pattern which is quite similar to the spatial distribution of A_h and not to B_h and B_v, which are compensating each other.

5.3. Investigation of a High IV Event

Figure 2b indicated that the potential temperature IV fluctuates in time with periods of low and high IV. For a more detailed investigation of the potential temperature IV and its contributions the focus is in the following on a time period with intense IV. We expect that the synoptic activity at time scales of 2–6 days impacts the IV, and we are interested to identify associated mechanisms. Therefore, 5 August 2012 at 06:00 UTC (coinciding with the great Arctic cyclone event) is chosen to analyze the individual contributions to the simulated IV. The results are shown at 500 hPa, because the IV reaches its maximum at this level (see Table 1). The spatial distribution highlights the locations of strong and weak IV occurrences (Figure 8a). Values of IV higher than $30\,K^2$ appear over two regions. The larger region ranges from the Laptev Sea to the Beaufort Sea and covers the Arctic Ocean. This center is quite intense and reaches down to the surface (not shown). The second and smaller center is located over the north of Greenland and Greenland Sea. During the 2 days prior the maximum event on 5 August 2012 at 06:00 UTC the two centers start to form from several small centers of high potential temperature IV. The center over Greenland grows faster, despite being the smaller one. After the maximum event both centers dissipate again into several small regions of intense IV (not shown).

The most relevant contributions are both baroclinic terms, B_h and B_v (Table 1 and Figures 8b and 8c). But, unlike the domain, vertical and temporal averaged results (Figures 4–7), both B_h and B_v can have positive and negative impacts on IV tendency of potential temperature, depending on the location (Figures 8b and 8c). Besides, the diabatic source and sink term C (Figure 8d) has an interesting regional influence on the IV tendency during this maximum IV event with absolute values comparable to B_h and B_v. The contributions to IV tendency of the other terms are negligible with A_h, A_v, and E_v reducing and E_h producing IV in domain and vertical average (see Table 1). On 5 August 2012 at 06:00 UTC, clear centers of strong positive contributions to potential temperature IV tendencies are found for B_h and C. Both reach values $>20\times10^{-5}K^2/s$ over the East Siberian Sea/Chukchi Sea that are compensated only by B_v (values $<-20\times10^{-5}K^2/s$). During this time step this region is characterized by low pressure and a high Eady growth rate (not shown) and coincides with the center of the great Arctic cyclone in the beginning of August 2012 [*Simmonds and Rudeva*, 2012; *Zhang et al*., 2013; *Parkinson and Comiso*, 2013]. The cyclone results in a strong sea ice retreat in this region [*Zhang et al*., 2013; *Parkinson and Comiso*, 2013]. Due to this sea ice loss the vertical fluxes of moisture and heat change between the ocean and the atmosphere. All ensemble members share the same anomalous sea ice concentration (given by the ERA-Interim data set) during this period. But, the atmospheric state (e.g., stability of the atmospheric boundary layer) is different between the individual ensemble members. Accordingly, turbulent and diabatic processes are different, explaining the high IV generated by the term C over this region. The sum of all terms (Figure 8h) largely reflects the pattern of the IV (Figure 8a).

6. Discussion and Conclusion

In this study the intermember variability (IV) generated in the HIRHAM5 regional atmospheric model over the Arctic was analyzed for the late summer season July–September 2012.

Our results support the argument expressed by *Rinke et al*. [2004] and *von Storch* [2005] that the IV in summer in the Arctic is generally stronger than in the midlatitudes due to strong temperature gradients and weak flow through the model domain resulting in a weaker control exerted by LBC. The pronounced IV points to the general limitation of a single realization for the Arctic unnudged simulations. A model evaluation compared with observations should therefore be focused on statistics based on ensemble simulations. Nudging helps to constrain the large-scale flow but has limited impact on Arctic RCM near-surface temperature and precipitation [*Berg et al*., 2013; *Glisan et al*., 2013].

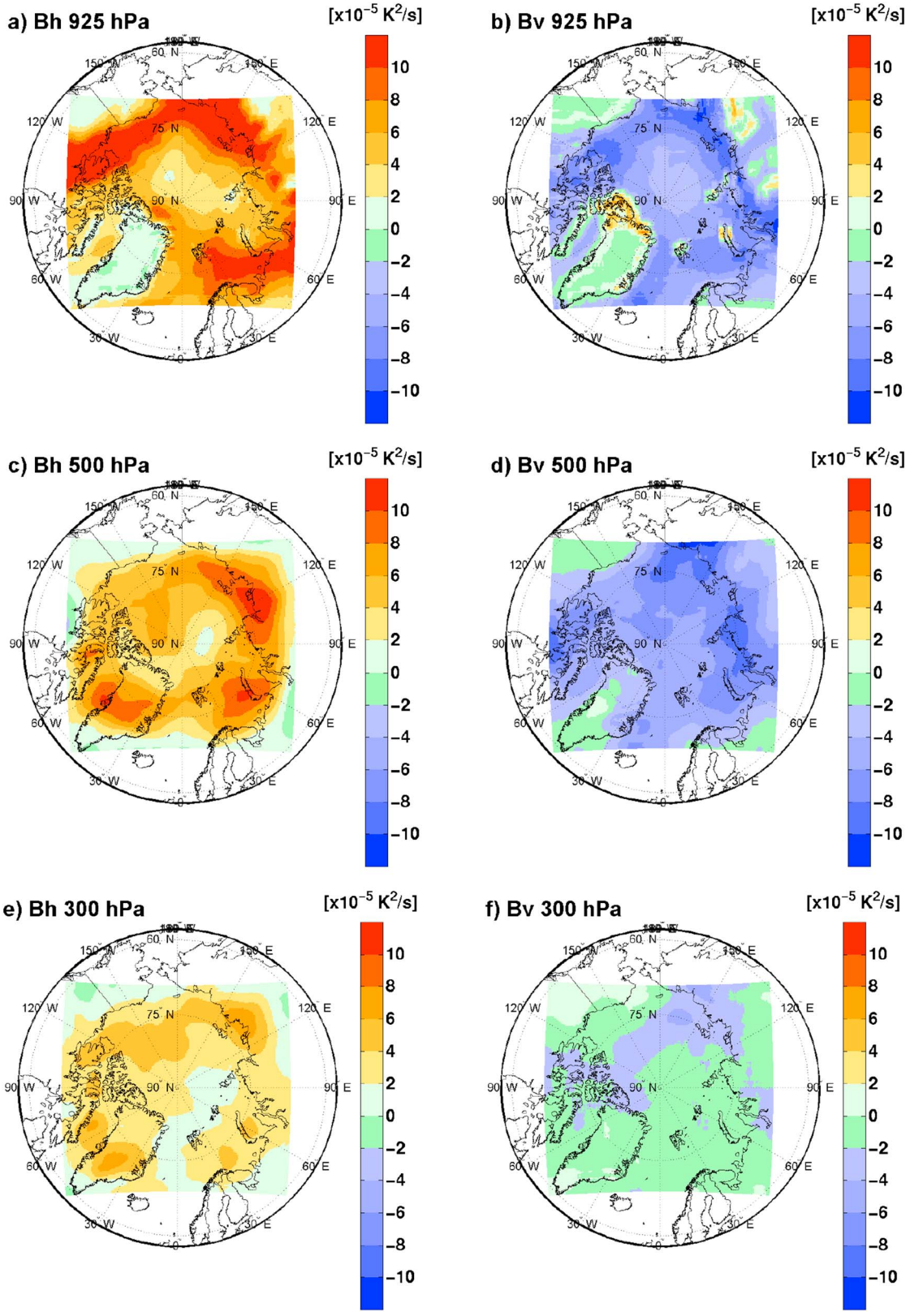

Figure 7. Temporal averaged contributions (first column) B_h and (second column) B_v in 10^{-5}K^2/s at (first row) 925 hPa, (second row) 500 hPa, and (third row) 300 hPa.

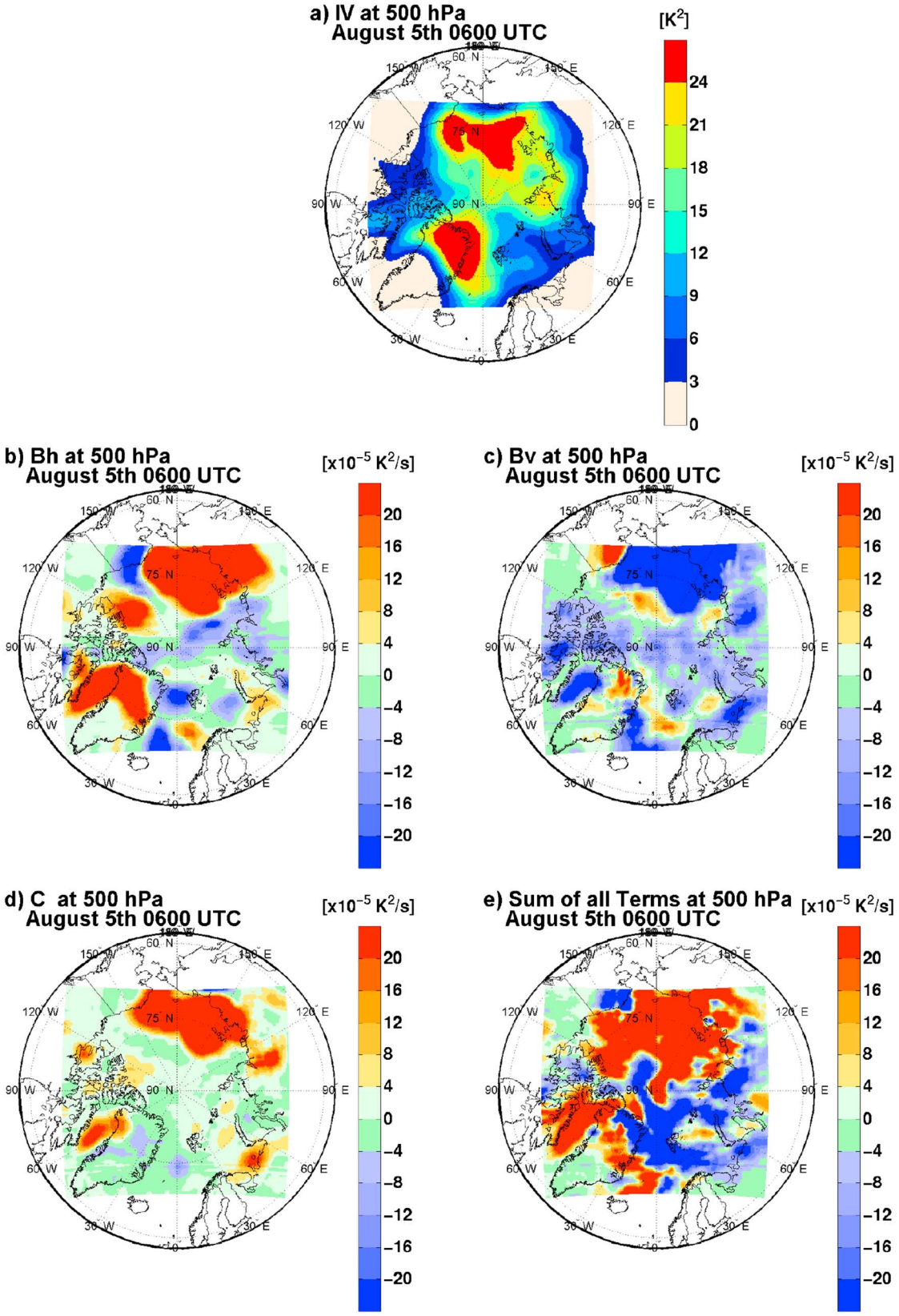

Figure 8. Intermember variability in (a) K^2 and terms (b) B_h, (c) B_v, and (d) C in 10^{-5}K^2/s and (e) the sum of all seven contributions in 10^{-5}K^2/s, all for 5 August at 06:00 UTC at 500 hPa.

The vertical profile of IV is similar to the results found by *NL*2010 with the Canadian RCM (CRCM5) covering the eastern part of northern America and parts of the Atlantic Ocean with strongest potential temperature IV in the midtroposphere and near the surface. However, the magnitude significantly differs between both studies. Over the Arctic the IV reaches values of up to 7 K^2, while *NL*2010 presented over their domain an IV with an intensity up to 100 times smaller than over the Arctic. Already *Rinke et al*. [2004] found that the IV over the Arctic is larger compared to the one over the midlatitudes. The same magnitude of difference (100 times) is observed for the vertical and domain-averaged IV in the Arctic and over North America. However, the temporal variability of IV is more pronounced over North America, leading to maximum IV events that are 5 times higher compared to low IV events [*NL*2010], whereas over the Arctic the IV differences between the high and low IV events are on the order of 3. In agreement with several previous studies [*Giorgi and Bi*, 2000; *Christensen et al*., 2001; *Caya and Biner*, 2004; *Rinke et al*., 2004; *Wu et al*., 2005; *Alexandru et al*., 2007; *Lucas-Picher et al*., 2008a; *NL*2010, 2011], we emphasize strong temporal variations of the IV. The time scale of these fluctuations ranges from a few days up to a week, thus covering the synoptic time scale.

For the Arctic and the analyzed time period from July to September 2012, the most important contributions to IV tendency of potential temperature are the horizontal and vertical baroclinic terms (B_h and B_v). The baroclinicity is related to the occurrence of cyclones whose frequency reaches its maximum on August, followed by July and September [*Serreze and Barry*, 1988]. Whereas the domain-averaged B_h has always positive values indicating a generation of IV, B_v has always negative values leading to a reduction of IV. Near the surface, the domain-averaged absolute values of B_h are higher than of B_v.

At 500 hPa both contributions are balancing each other, while at 300 hPa the contribution to IV tendency is dominated by B_h. While the term C contributes to compensate B_h near the surface and therefore reduces the IV tendency, in the midtroposphere C contributes to a generation of IV. Apart from the horizontal transport term A_h with enhanced importance with increasing height, the other terms have insignificant contributions to the potential temperature IV tendency in general (A_v and E_v). They can contribute positively and negatively to IV tendency depending on the location, leading to a balance over the model domain (A_h and E_h). Compared to the study over northern America [*NL*2010] we find the agreement that B_h contributes positively and B_v negatively and have the strongest influence near the surface. However, in contrast to our Arctic study, northern America is characterized by a diabatic source and sink term C that contributes to a generation of IV tendency near the surface and has an important influence even near the tropopause. With increasing height the horizontal transport term (A_h) gets more important and the influence of B_h is reduced [*NL*2010]. The spatial distribution of the vertical and temporal averaged seven contribution terms shows distinct spatial patterns indicating that terms can contribute positively or negatively depending on the regions. B_h and B_v have a large magnitude along the coastline of the Arctic Ocean in the lower and middle troposphere. This belt of high baroclinic contribution to IV tendency is in agreement with the Arctic frontal zone at the Arctic Ocean coastline discussed by *Serreze et al*. [2001]. The frontal zones at the coastlines during summer are explained by a strong temperature gradient between the cold Arctic Ocean and the relatively warm snow-free land and by wind maxima in the upper troposphere [*Serreze et al*., 2001]. In addition, *Serreze and Barrett* [2008] found that most cyclones have their origin during summer rather over Eurasia than over North America and the northern Pacific.

Considering the event of maximum IV (5 August 2012 at 06:00 UTC) the horizontal baroclinic term B_h contributes strongest to its growth, related to the great Arctic cyclone event at the beginning of August 2012. Two regional centers of high IV (up to 30 K^2) are established by contributions due to B_h and C and its reduction due to B_v. The term C plays a role because of the cyclone-driven changed exchange of moisture and heat between the atmosphere and the ocean. This is partly in contrast to the results obtained by *NL*2010 for North America. They found that the event of maximum IV reveals the strongest reduction of IV due to B_v as well but is mainly generated by the diabatic source and sink term C only and not due to B_h as in the Arctic.

This study reveals the distinct IV and its contributions over the circum Arctic domain. There is agreement that the IV and the influencing processes are a function of the considered model domain and the corresponding atmospheric dynamics. However, an insensitivity of IV to the applied RCM in the Arctic was found (Nikiema et al., Chaos in regional climate model simulations over the Arctic domain: Comparison of intermember variability in ensemble simulations of CRCM5 and HIRHAM5 models, submitted to *Polarforschung*, 2015). They applied the diagnostic budget study over the circum Arctic domain comparing the results obtained with

the HIRHAM5 with the results of the CRCM5. Both models cover the same model domain and time period and use the same LBC and the same method to generate the ensemble of 20 members. The IV and its dynamical and diabatic contributions reveal quite similar results with respect to the vertical profile, temporal evolution, and spatial distribution.

Despite the fact that 2012 was an extreme year concerning the summer sea ice retreat, the presented results are representative for the Arctic summer IV. We investigated additional years (2006, 2007, and 2009) and found very similar results for the IV and its dynamical and diabatic contributions (Figure S2). A detailed investigation of the potential impact of regional sea ice loss on spatial and temporal patterns of IV is in preparation. The pronounced internally generated variability, particularly in summer and early autumn, has been discussed for coupled atmosphere-ice-ocean Arctic RCMs as well by *Döscher et al*. [2010], *Dorn et al*. [2012], and *Rinke et al*. [2013]. But, the role of regional sea ice anomalies for the internally generated model variability has still to be clarified.

The investigation of the potential temperature IV is the first step to quantify the IV generated over the Arctic with HIRHAM5. Further, it is necessary to consider other variables like the absolute and relative vorticity [*NL*2010, 2011] and extend this study to a whole energy cycle associated with IV [*Nikiema and Laprise*, 2013; *Nikiéma and Laprise*, 2015].

Acknowledgments
This study was funded by the Helmholtz Climate Initiative REKLIM and is part of the dissertation (Sommerfeld A., Quantification of internal variability of the Arctic summer atmosphere based on HIRHAM5 ensemble simulations, University Potsdam, Germany, 2015). The simulations with the HIRHAM5 were performed at the German Climate Computing Center (DKRZ, Hamburg). For data access, please contact anja.sommerfeld@awi.de. The authors thank Ines Hebestadt for the technical support concerning the HIRHAM5.

References

Alexandru, A., R. de Elía, and R. Laprise (2007), Internal variability in regional climate downscaling at the seasonal scale, *Mon. Weather Rev.*, *135*, 3221–3238, doi:10.1175/MWR3456.1.

Bellprat, O., S. Kotlarski, D. Lüthi, and C. Schär (2012), Exploring perturbed physics ensembles in a regional climate model, *J. Clim.*, *25*, 4582–4599, doi:10.1175/JCLI-D-11-00275.1.

Berg, P., R. Döscher, and T. Koenigk (2013), Impacts of using spectral nudging on regional climate model RCA4 simulations of the Arctic, *Geosci. Model Dev.*, *6*, 849–859, doi:10.5194/gmd-6-849-2013.

Bonavita, M., L. Raynaud, and L. Isaksen (2011), Estimating background-error variances with the ECMWF ensemble of data assimilations system: Some effects of ensemble size and day-to-day variability, *Q. J. R. Meteorol. Soc.*, *137*, 423–434, doi:10.1002/qj.756.

Buizza, R., and T. N. Palmer (1995), The singular-vector structure of the atmospheric general circulation, *J. Atmos. Sci.*, *52*(9), 1434–1456.

Caya, D., and S. Biner (2004), Internal variability of RCM simulations over an annual cycle, *Clim. Dyn.*, *22*, 33–46, doi:10.1007/s00382-003-0360-2.

Christensen, O. B., M. A. Gaertner, J. A. Prego, and J. Polcher (2001), Internal variability of regional climate models, *Clim. Dyn.*, *17*, 875–887, doi:10.1007/s003820100154.

Christensen, O. B., M. Drews, J. H. Christensen, K. Dethloff, K. Ketelsen, I. Hebestadt, and A. Rinke (2007), Technical report 06–17, The HIRHAM Regional Climate Model Version 5 (β).

Collins, M. (2007), Ensembles and probabilities: A new era in the prediction of climate change, *Philos. Trans. R. Soc. A*, *365*, 1957–1970, doi:10.1098/rsta.2011.0307.

Crétat, J., and B. Pohl (2012), How physical parameterizations can modulate internal variability in a regional climate model, *J. Atmos. Sci.*, *69*, 714–724.

Dee, D. P., S. M. Uppala, A. J. Simmons, P. Berrisford, P. Poli, S. Kobayashi, U. Andrae, M. A. Balmaseda, G. Balsamo, and P. Bauer (2011), The ERA-Interim reanalysis: Configuration and performance of the data assimilation system, *Q. J. R. Meteorol. Soc.*, *137*, 553–597, doi:10.1002/qj.828.

Dorn, W., K. Dethloff, and A. Rinke (2012), Limitations of a coupled regional climate model in the reproduction of the observed Arctic sea-ice, retreat, *Cryosphere*, *6*, 985–998, doi:10.5194/tc-6-985-2012.

Döscher, R., K. Wyser, M. Meier, M. Qian, and R. Redler (2010), Quantifying Arctic contributions to climate predictability in a regional coupled ocean-ice-atmosphere model, *Clim. Dyn.*, *34*, 1157–1176, doi:10.1007/s00382-009-0567-y.

Evans, J. P., F. Ji, G. Abramowski, and M. Ekström (2013), Optimally choosing small ensemble members to produce robust climate simulations, *Environ. Res. Lett.*, *8*, 4, doi:10.1088/1748-9326/8/4/044050.

Giorgi, F., and X. Bi (2000), A study of internal variability of a regional climate model, *J. Geophys. Res.*, *105*, 29,503–29,521, doi:10.1029/2000JD900269.

Glisan, J. M., W. J. Gutowski Jr., J. J. Cassano, and M. E. Higgins (2013), Effects of spectral nudging in WRF on Arctic temperature and precipitation simulations, *J. Clim.*, *26*, 3985–3999, doi:10.1175/JCLI-D-12-00318.1.

Gneiting, T., and A. E. Raftery (2005), Weather forecasting with ensemble methods, *Science*, *310*, 248–249.

Hawkins, E., and R. Sutton (2009), The potential to narrow uncertainty in regional climate predictions, *Bull. Am. Meteorol. Soc.*, *90*, 1095–1107, doi:10.1175/2009BAMS2607.1.

Houtekamer, P. L., L. Lefaivre, J. Derome, H. Ritchie, and H. Mitchell (1996), A system simulation approach to ensemble prediction, *Mon. Weather Rev.*, *124*, 1225–1242.

Jaiser, R., K. Dethloff, D. Handorf, A. Rinke, and J. Cohen (2012), Impact of sea ice cover changes on the Northern Hemisphere atmospheric winter circulation, *Tellus*, *64*, doi:10.3402/tellusa.v64i0.11595.

Klaus, D., W. Dorn, K. Dethloff, A. Rinke, and M. Mielke (2012), Evaluation of two cloud parameterizations and their possible adaptation to Arctic climate conditions, *Atmosphere*, *3*, 419–450, doi:10.3390/atmos3030419.

Kunii, M. (2014), The 1000-member ensemble Kalman filtering with the JMA nonhydrostatic mesoscale model on the K computer, *J. Meteorol. Soc. Jpn.*, *92*(6), 623–633, doi:10.2151/jmsj.2014-607.

Lucas-Picher, P., D. Caya, R. de Elía, and R. Laprise (2008a), Investigation of regional climate models' internal variability with a ten-member ensemble of 10-year simulations over a large domain, *Clim. Dyn.*, *31*, 927–940, doi:10.1007/s00382-008-0384-8.

Lucas-Picher, P., D. Caya, S. Biner, and R. Laprise (2008b), Quantification of the lateral boundary forcing of a regional climate model using an aging tracer, *Mon. Weather Rev.*, *136*, 4980–4996, doi:10.1175/2008MWR2448.1.

Mullen, S. L., and R. Buizza (2002), The impact of horizontal resolution and ensemble size on probabilistic forecasts of precipitation by the ECMWF ensemble prediction system, *Weather Forecasting*, *17*, 173–191, doi:10.1175/1520-0434(2002)017<0173:TIOHRA>2.0.CO.2.

Nikiema, O., and R. Laprise (2010), Diagnostic budget study of the internal variability in ensemble simulations of the Canadian RCM, *Clim. Dyn.*, *36*, 2313–2337, doi:10.1007/s00382-010-0834-y.
Nikiema, O., and R. Laprise (2011), Budget study of the internal variability in ensemble simulations of the Canadian Regional Climate Model at the seasonal scale, *J. Geophys. Res.*, *116* D16112, doi:10.1029/2011JD015841.
Nikiema, O., and R. Laprise (2013), An approximate energy cycle for inter-member variability in ensemble simulations of a regional climate model, *Clim. Dyn.*, *41*, 831–852, doi:10.1007/s00382-012-1575-x.
Nikiéma, O., and R. Laprise (2015), Energy cycle associated with inter-member variability in a large ensemble of simulations with the Canadian RCM (CRCM5), *Clim. Dyn.*, doi:10.1007/s00382-015-2604-3.
O'Brien, T. A., L. C. Sloan, and M. A. Snyder (2011), Can ensembles of regional climate model simulations improve results from sensitivity studies?, *Clim. Dyn.*, *37*, 1111–1118, doi:10.1007/s00382-010-0900-5.
Parkinson, C. L., and J. C. Comiso (2013), On the 2012 record low Arctic sea ice cover: Combined impact of preconditioning and an August storm, *Geophys. Res. Lett.*, *40*, 1356–1361, doi:10.1002/grl.50349.
Porter, D. F., J. J. Cassano, and M. C. Serreze (2012), Local and large-scale atmospheric response to reduced Arctic sea ice and ocean warming in the WRF model, *J. Geophys. Res.*, *117* D11115, doi:10.1029/2011JD016969.
Rinke, A., and K. Dethloff (2000), On the sensitivity of a regional Arctic climate model to initial and boundary conditions, *Clim. Res.*, *14*, 101–113.
Rinke, A., P. Marbaix, and K. Dethloff (2004), Internal variability in Arctic regional climate simulations: Case study for the SHEBA year, *Clim. Res.*, *27*, 197–209.
Rinke, A., K. Dethloff, W. Dorn, D. Handorf, and J. C. Moore (2013), Simulated Arctic atmospheric feedbacks associated with late summer sea ice anomalies, *J. Geophys. Res. Atmos.*, *118*, 7698–7714.
Roeckner, E., et al. (2003), The atmospheric general circulation model ECHAM5-Part 1: Model description, Technical Report 349, Max-Planck-Institute (MPI) for Meteorology: Hamburg, Germany.
Roesch, A., E. B. Jaeger, D. Lüthi, and S. I. Seneviratne (2008), Analysis of CCLM model biases in relation to intra-ensemble model variability, *Meteorol. Z.*, *17*(4), 369–382, doi:10.1127/0941-2948/2008/0307.
Sasse, R., and G. Schädler (2014), Generation of regional climate ensembles using Atmospheric Forcing Shifting, *Int. J. Climatol.*, *34*, 2205–2217, doi:10.1002/joc.3831.
Serreze, M. C., and A. P. Barrett (2008), The summer cyclone maximum over the central Arctic Ocean, *J. Clim.*, *21*, 1048–1065, doi:10.1175/2007JCLI1810.1.
Serreze, M. C., and R. G. Barry (1988), Synoptic activity in the Arctic Basin, 1979–85, *J. Clim.*, *1*, 1276–1295.
Serreze, M. C., A. H. Lynch, and M. P. Clark (2001), The Arctic Frontal Zone as seen in the NCEP-NCAR reanalysis, *J. Clim.*, *14*, 1550–1567.
Simmonds, I., and I. Rudeva (2012), The great Arctic cyclone of August 2012, *Geophys. Res. Lett.*, *39* L23709, doi:10.1029/2012GL054259.
Theis, S., and C. Gebhardt (2009), Fundamentals of ensemble technique and probability statements, in *Promet - Modern Methods and Tools of the Weather Forecast at the German Weather Service* [in German], edited by J. Rapp, pp. 104–110, Deutscher Wetterdienst in Offenbach, Germany.
Toth, Z., and E. Kalnay (1993), Ensemble forecasting at NMC: The generation of perturbations, *Bull. Am. Meteorol. Soc.*, *74*, 2317–2330.
Troccoli, A., and T. N. Palmer (2007), Ensemble decadal prediction from analysed initial conditions, *Philos. Trans. R. Soc. A*, *365*, 2179–2191, doi:10.1098/rsta.2007.2079.
Undén, P., L. Rontu, H. Järvinen, P. Lynch, J. Calvo, G. Cats, J. Cuxart, K. Eerola, C. Fortelius, and J. A. Garcia-Moya (2002), HIRLAM-5 Scientific Documentation., HIRLAM-5 Project, Swedish Meteorological and Hydrological Institute (SMHI): Norrköping, Sweden.
von Storch, H. (2005), Models of global and regional climate, in *Encyclopedia Hydrological Science Meteorology and Climatology*, vol. 1, edited by M. G. Anderson, pp. 478–490, John Wiley.
Wan, H., R. J. Rasch, K. Zhang, Y. Qian, H. Yan, and C. Zhao (2014), Short ensembles: An efficient method for discerning climate-relevant sensitivities in atmospheric general circulation models, *Geosci. Model Dev.*, *7*, 1961–1977, doi:10.5194/gmd-7-1961-2014.
Wu, W., A. H. Lynch, and A. Rivers (2005), Estimating the uncertainty in a regional climate model related to initial and lateral boundary conditions, *J. Clim.*, *18*, 917–931, doi:10.1175/JCLI-3293.1.
Zhang, J., R. Lindsay, A. Schweiger, and M. Steele (2013), The impact of an intense summer cyclone on 2012 Arctic sea ice retreat, *Geophys. Res. Lett.*, *40*, 720–726, doi:10.1002/grl.50190.
Zhou, X., H. Matthes, A. Rinke, K. Klehmet, B. Heim, W. Dorn, D. Klaus, K. Dethloff, and B. Rockel (2014), Evaluation of Arctic land snow cover characteristics, surface albedo, and temperature during the transition seasons from regional climate model simulations and satellite data, *Adv. Meteorol* 604157, doi:10.1155/2014/604157.